Journal of Crystal Growth 570 (2021) 126235

Contents lists available at ScienceDirect

Journal of Crystal Growth

journal homepage: www.elsevier.com/locate/jcrysgro

Unraveling the structural and electronic properties of strained PbSe on GaAs

X. Liu [a], J. Wang [a], L. Riney [a], S.K. Bac [a], David J. Smith [b], M.R. McCartney [b], I. Khan [c], A. J. Hoffman [c], M. Dobrowolska [a], J.K. Furdyna [a], B.A. Assaf [a,*]

[a] Department of Physics, University of Notre Dame, Notre Dame, IN, 46556, USA
[b] Department of Physics, Arizona State University, Tempe, AZ 85287, USA
[c] Department of Electrical Engineering, University of Notre Dame, Notre Dame, IN 46556, USA

ARTICLE INFO

Keyword:
A1. X-ray Diffraction
A1. Interfaces
A1. Transmission Electron Microscopy
A3. Molecular beam epitaxy
B2. Semiconducting lead compounds
B2. Topological insulators

ABSTRACT

Thin films of PbSe have been synthesized by molecular beam epitaxy on both GaAs(100) and GaAs(111)B substrates. Despite the smaller lattice constant of GaAs, the PbSe layers are (001)-oriented and undergo in-plane tensile strain on both substrates due to the thermal expansion coefficient mismatch between the materials. High resolution transmission electron microscopy observations reveal an abrupt and highly crystalline interface, not impacted by the tensile strain. The impact of strain on the electronic band structure is computed and found to induce an increase in the energy gap by as much as 10%.

1. Introduction

The IV-VI (Pb,Sn) chalcogenides are exciting material systems that host a combination of unique quantum properties. For example, a topological phase protected by crystalline symmetry has recently been discovered [1,2,3,4]. This state co-exists with well-known characteristics that make these materials useful for infrared devices [5,6] and thermoelectric applications [7,8,9]. The synthesis of $Pb_{1-x}Sn_xSe$ and $Pb_{1-x}Sn_xTe$ films is most commonly done on BaF_2 substrates and buffer layers, [10] which have an ultrawide band gap (11 eV) and are closely lattice-matched [11]. Growth on large wafer substrates such as GaAs, InAs and InP would be highly advantageous for device applications since these substrates are better adapted to processing tools. The lattice constant of rocksalt PbSe (6.124 Å) is only slightly mismatched with that of zincblende InAs (6.058 Å), but is more than 7.7% larger than that of zincblende GaAs (5.653 Å).

Previously investigated in the context of infrared devices, [12,13,14,15] the growth of IV-VI semiconductors on the more mainstream III-V substrates has been recently revisited [16]. In these works, PbSe growth on GaSb and InAs was studied with particular focus on the atomic arrangements at the interface, yielding a good understanding of how PbSe islands nucleate and grow on these substrates [16]. In previous work, control of the lattice orientation of PbSe was also studied [14,17]. The impact of thermal strain (on PbTe) was even considered, [18] and was shown to result in a discontinuous layer that impacted transport properties in the case of thick epilayers. However, its impact on the electronic structure was never studied. $Pb_{1-x}Sn_xTe$ films have also been grown on GaAs to realize induced superconductivity by proximity but the nature of the substrate–layer interface was not considered [19]. Most previous studies have focused on structural characteristics but a combined look at how structure correlates with electronic properties is still lacking. As for the numerous heteroepitaxial interfaces [20,21,22,23,24,25,26] studied in the past, the IV-VI/III-V heterointerface can enable strain and charge tuning not possible with BaF_2. Hence, IV-VI/III-V growth remains a subject of ongoing research.

Motivated by this fact, we have synthesized rocksalt PbSe thin films on (001) and (111) GaAs zincblende substrates. GaAs has a −7.7% lattice mismatch with PbSe and thermal expansion coefficient smaller by about a factor of 4 near room temperature. Despite these differences, a sharp interface is formed with very few threading dislocations propagating into the bulk of the deposited PbSe epilayers. Interestingly, growth on the (001) and (111)B GaAs surfaces both yielded (001)-oriented PbSe layers that are under biaxial in-plane tensile strain resulting from the thermal expansion coefficient mismatch between PbSe and GaAs. We also show that this type of strain can also increase the energy gap of PbSe by as much as 10% of its room temperature value, a finding that is relevant to future advances on tunable infrared devices and fundamental studies on the topological nature of IV-VI materials.

* Corresponding author.
E-mail address: bassaf@nd.edu (B.A. Assaf).

https://doi.org/10.1016/j.jcrysgro.2021.126235
Received 17 April 2021; Received in revised form 3 June 2021; Accepted 11 June 2021
Available online 25 June 2021

2. Sample synthesis

The PbSe epilayers (≥100 nm) were grown by molecular beam epitaxy on GaAs (0 0 1) and (1 1 1)B substrates. The substrates were initially heated to 600 °C to desorb the surface oxide while the surface was monitored using reflection high-energy electron diffraction (RHEED). A GaAs buffer layer was then grown on the (0 0 1) substrates. The GaAs (1 1 1)B substrates undergo a Se surface treatment prior to growth, which is necessary to obtain a smooth surface [31]. The substrate temperature is held at 350 °C (300 °C for Sample C) during the PbSe growth. A compound PbSe source was used together with a persistent Se flux. The structural properties of all samples are reported in Table 1. The layers were characterized using high-resolution X-ray diffraction (HRXRD) and cross-sectional transmission electron microscopy (TEM).

3. Results

3.1. PbSe on GaAs (100)

Fig. 1(a) shows an XRD reciprocal space map obtained near the GaAs (0 0 4) peak. The PbSe (0 0 4) peak is visible nearby, and results in a perpendicular lattice constant $a_{\perp} = 6.122 \pm 0.002$Å. A reciprocal space map taken near the (1 1 5) peak of GaAs is shown in Fig. 1(b). The PbSe peak recovered from this map yields an in-plane lattice constant $a_{||}$= 6.15 ± 0.01 Å indicating that the layer is under in-plane tensile strain. This strain is due to the large thermal expansion coefficient of PbSe, almost four times large than that of GaAs [12,32]. Upon cooldown, GaAs contracts at a rate smaller than that of PbSe, thus yielding the net tensile strain, due to the mismatch between the contraction (expansion) rates of the two materials. A ϕ-scan performed about the (1 1 5) Bragg peak is shown in Fig. 1(c). The 4-fold symmetry of PbSe is preserved and aligns with the 4-fold symmetry of the same GaAs peak. We conclude that a [1 0 0] || [1 0 0] in-plane alignment occurs between the two materials. The larger broadening of the PbSe Bragg peak along the [1 1 0] direction (parallel to the interface) compared to the substrate can be related to the smaller lateral correlation length of PbSe, yielding a large distribution of in-plane atomic spacings at the interface. This can be due to the occurrence of misfit dislocations at the PbSe/GaAs interface, as will be shown below.

To quantify the amount of strain, we rely on the in-plane lattice constant, which is generally more impacted by stress than the out-of-plane lattice constant for IV-VI materials. This consequence of the fact that [33]:

$$\varepsilon_{\perp} = -2\frac{C_{12}}{C_{11}}\varepsilon_{||} \approx -0.31\varepsilon_{||} \quad (1)$$

C_{12} and C_{11} are the elastic constants listed in Table 2 for PbSe.$\varepsilon_{\perp} = (a_{\perp} - a_0)/a_0$ and $\varepsilon_{||} = (a_{||} - a_0)/a_0$ quantify out-of-plane and in-plane strain, respectively. We utilize Eq. (1) to solve for $a_0 \approx 6.13 \pm 0.01$. This is the unstrained lattice constant extracted from our experiment. It agrees with the bulk lattice constant within error [27,28,29,30]. The values of $\varepsilon_{\perp}$ and $\varepsilon_{||}$ recovered using a_0 are shown in Table 1. The uncertainty of both quantities is relatively large. However, as shown later, only $\varepsilon_{||}$ has a significant impact on the energy band structure. $\varepsilon_{||} = (0.33 \pm 0.2)\%$ for sample A grown on GaAs(0 0 1).

Transmission electron micrographs of Sample A near the interface are shown in Fig. 2(a-f). The aberration-corrected annular-dark-field image in Fig. 2(a) shows the atomically-resolved structure of the interface and indicates excellent epitaxial growth, as shown by alignment of the [1 1 0] directions in the two layers. The Fourier-filtered image shown in Fig. 2(b) reveals the presence of an array of discontinuities along the interface. The enlargement in Fig. 2(c) of a nearby region shows that these faults occur at positions where the Pb atomic columns in PbSe (shown in blue) do not line up with the underlying As atomic columns (shown in orange). From Fig. 2(b, c), we also conclude that the locations of the Pb atomic columns in the first PbSe monolayer with respect to the As atomic columns are not uniform.

Four intensity line profiles perpendicular to the interface are taken at two different locations indicated in Fig. 2(a), and are shown in Fig. 2(d). The green and orange lines are taken over an area where the Pb column is directly above the As column and the red and blue are over an area where it is not. We note that the vertical position of the top atomic layer of the GaAs substrate (seen in Fig. 2(c)) along with intensity analysis based on atomically-resolved images of the substrate confirm that an As-terminated surface has been formed (Fig. 2(d)). In between positions exhibiting discontinuities, the Pb columns are located almost directly above the As columns. However, it appears that the Pb atoms near a defect line can glide freely on the surface, completely ignoring the underlying As plane. This picture can be contrasted with what was observed for PbSe(0 0 1) grown on InAs(0 0 1), where Pb atomic columns were found to be directly above those of As [16]. The peak amplitudes in Fig. 2(d) and their spacings with respect to nearest neighbors allows their elemental nature to be determined. The checker-board repetition within the PbSe layer, is as expected for the rocksalt structure. By comparing the red and orange line profiles, both Pb and Se atomic columns can be identified in the first PbSe layer. This is an indication that PbSe forms neutral pairs even at the first monolayer (ML), and likely nucleates at random locations on the substrate surface.

Intensity line profiles taken in the direction parallel to the interface are shown in Fig. 2(e). Peaks of intensity at the first ML are mostly out-of-phase with those in the second ML immediately above. While some disorder is visible in this first ML, it does not seem to impact the second ML, even at positions where the Pb atomic columns are not lined up with As atomic columns. Thus, it is evident that first few ML and structure of PbSe are pristine. This result shows that we have achieved a highly abrupt GaAs/PbSe interface with a heteroepitaxial [1 0 0] || [1 0 0] alignment. The most significant source of disorder is likely due to

Table 1
Properties of the four films studied in this work. The thickness was determined by TEM imaging and/or the Scherrer broadening of the Bragg peaks. All PbSe layers grown on GaAs are (0 0 1)-oriented. The lattice constants are measured using high resolution X-ray diffraction. The strain is determined by comparing to the experimental unstrained lattice constant $a_0 = 6.13 \pm 0.01$Å (±0.015 *for sample B*) which agrees with the bulk lattice constant $a = 6.124 - 6.126$ Å [27,28,29,30] within error. The uncertainties on $\varepsilon_{||,\perp}$ are propagated from that on a_0.

Sample	Substrate	Thickness	Lattice constant	ε
A	GaAs (1 0 0) + no treatment $T_{subs} = 350$ °C	160 nm TEM 180 nm Scherrer	$a_{\perp} = 6.122 \pm 0.002$ Å $a\|\| = 6.15 \pm 0.01$ Å	$\varepsilon_{\perp} = (-0.1 \pm 0.2)\%\varepsilon_{||} = (0.33 \pm 0.2)\%$
B	GaAs (1 1 1) + Se treatment $T_{subs} = 350$ °C	160 nm Scherrer	$a_{\perp} = 6.123 \pm 0.002$ Å $a\|\| = 6.16 \pm 0.015$ Å	$\varepsilon_{\perp} = (-0.10 \pm 0.25)\%\varepsilon_{||} = (0.49 \pm 0.25)\%$
C	GaAs (1 1 1) + Se treatment $T_{subs} = 300$ °C	350 nm TEM 380 nm Scherrer	$a_{\perp} = 6.123 \pm 0.002$ Å	
D	BaF_2 (1 1 1) $T_{subs} = 350$ °C	250 nm	$a_{\perp} = 6.124 \pm 0.002$ Å	

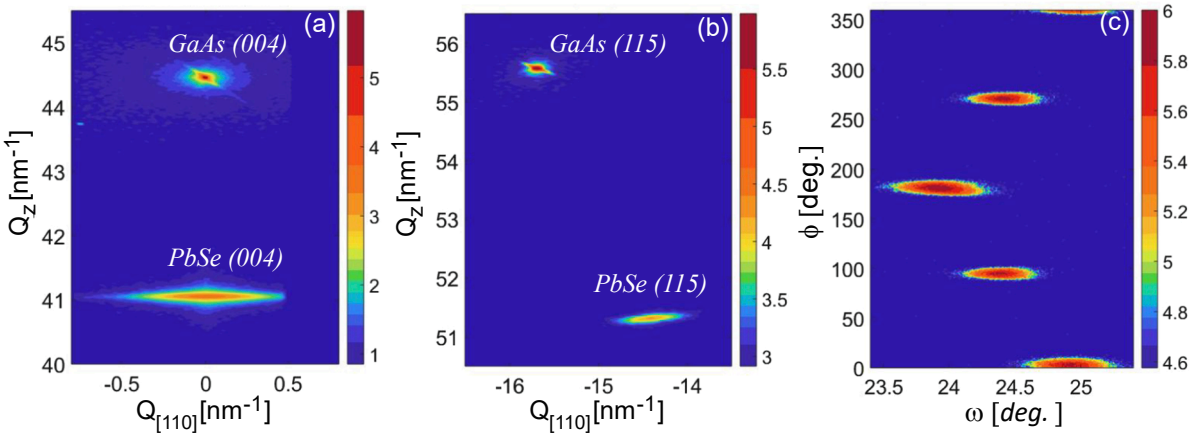

Fig 1. (a) High-resolution XRD space map of the (0 0 4) Bragg peak of GaAs and PbSe. (b) Asymmetric (1 1 5) Bragg reflection of PbSe and GaAs. (c) ϕ −scan of the (1 1 5) PbSe Bragg peak.$Q_z = 2\pi l/a$ and $Q_{[110]} = 2\pi\left(h^2 + k^2\right)^{1/2}/a$. a is the lattice parameter of GaAs and h, k *and* l the Miller indices.

Table 2
$D_u^{c,v}$ and $D_d^{c,v}$ the deformation potentials and C_{ij} the elastic constants of PbSe. c,v denote the conduction and valence band.

Deformation potentials (eV)	D_u^c	D_u^v	D_d^c	D_d^v
Ref. [39]	4.2	3.9	−4.2	−4.7
Elastic constants	C_{11}	C_{12}	C_{44}	
Ref. [33]	12.37	1.93	1.59	

arbitrary nucleation sites causing individual crystallites to start growing and merge randomly at different locations in the layer. This is confirmed by Fig. 2(f) showing multiple crystallites that have nucleated at arbitrary positions at the surface.

3.2. PbSe on GaAs (1 1 1)B

The structural properties of PbSe(0 0 1) grown on GaAs(1 1 1)B are next described. Fig. 3(a) shows an XRD pattern obtained for Sample B grown on a GaAs (1 1 1)B substrate. A strong (0 0 4) PbSe peak is observed, indicating that a (0 0 1)-oriented PbSe layer is obtained despite the (1 1 1) GaAs surface normal. The resulting out-of-plane lattice constant (6.123 Å) is slightly smaller than the bulk lattice constant of PbSe. The in-plane lattice constant extract from the XRD reciprocal space map shown in Fig. 3(b) is found to be $a_{||}$=6.16 ± 0.015 Å again indicating that the layer is under bi-axial in-plane tensile strain. We find that $\varepsilon\| = (0.49 \pm 0.25)\%$ for this sample. A φ-scan is also performed about a (1 3 5) GaAs Bragg peak (Fig. 3(c)) and a (1 1 5) PbSe peak (Fig. 3 (d)). The expected 6-fold symmetry of GaAs (1 1 1) is recovered, although a 24-fold symmetric reflection pattern is visible about the PbSe peak. The RHEED pattern obtained from PbSe grown on GaAs (1 1 1) (Fig. 3(e)) also shows two closely spaced streaks corresponding to two lattice spacings: a and $\sqrt{2}a$. This suggests the presence of a mixing of two types of rotated domains.

TEM images from the Sample C are shown in Fig. 4, and provide further understanding of the heteroepitaxial alignment of PbSe(1 0 0) on GaAs(1 1 1). The PbSe-GaAs interface is visible in Fig. 4(a) taken as a projection along the GaAs [1 1 0]direction. This image shows a surprising alignment where the [0 1 0]direction of PbSe ($\Delta a = 3.06A$) is along the $[\bar{1}12]$ direction on the GaAs(1 1 1) surface ($(\Delta a = 3.42A)$ along red arrows in Fig. 4(b)).

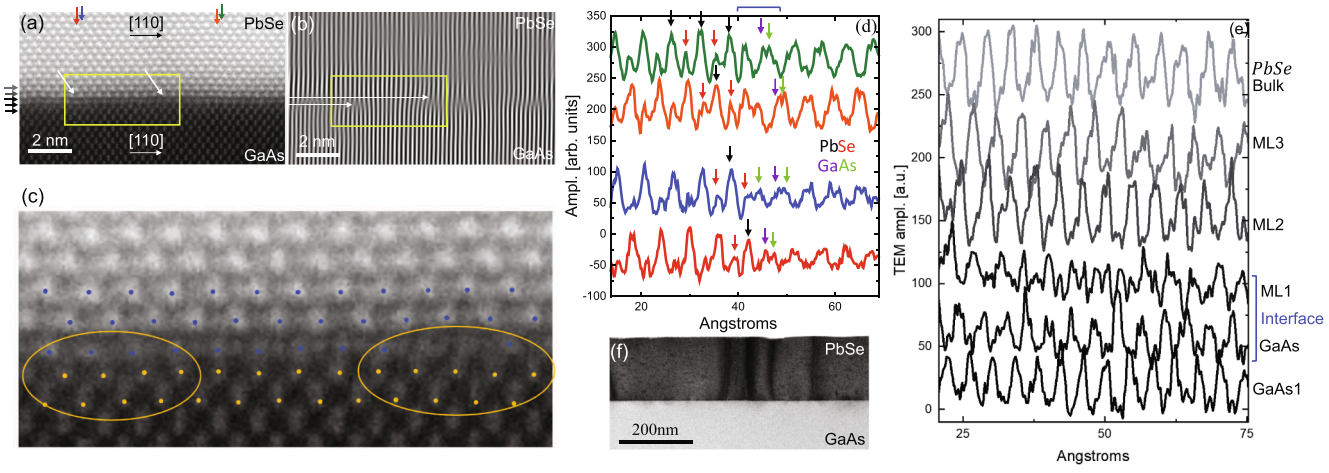

Fig 2. (a) Aberration-corrected annular-dark-field images of PbSe grown on GaAs (0 0 1). (b) Fourier-filtered image showing discontinuities across the interface. (c) Atomically-resolved image of the PbSe/GaAs interface. Blue dots mark Pb atomic columns while orange dots mark As atomic columns. The two orange circles mark areas where defects are observed. (d) Vertical line profiles taken at 4 positions indicated in (a). The interface is marked by the blue bracket. The As termination of the (0 0 1) surface is followed by either Pb or Se in the PbSe layer. A background intensity is subtracted here to account for differences in intensity levels between the GaAs and PbSe. (e) Horizontal line profiles near the interface showing the atomic periodicity of the GaAs layer, the first three ML of PbSe, and the bulk GaAs layer. (f) Lower magnification image showing grain boundaries and some dislocations near the substrate. (For interpretation of the references to colour in this figure legend, the reader is referred to the web version of this article.)

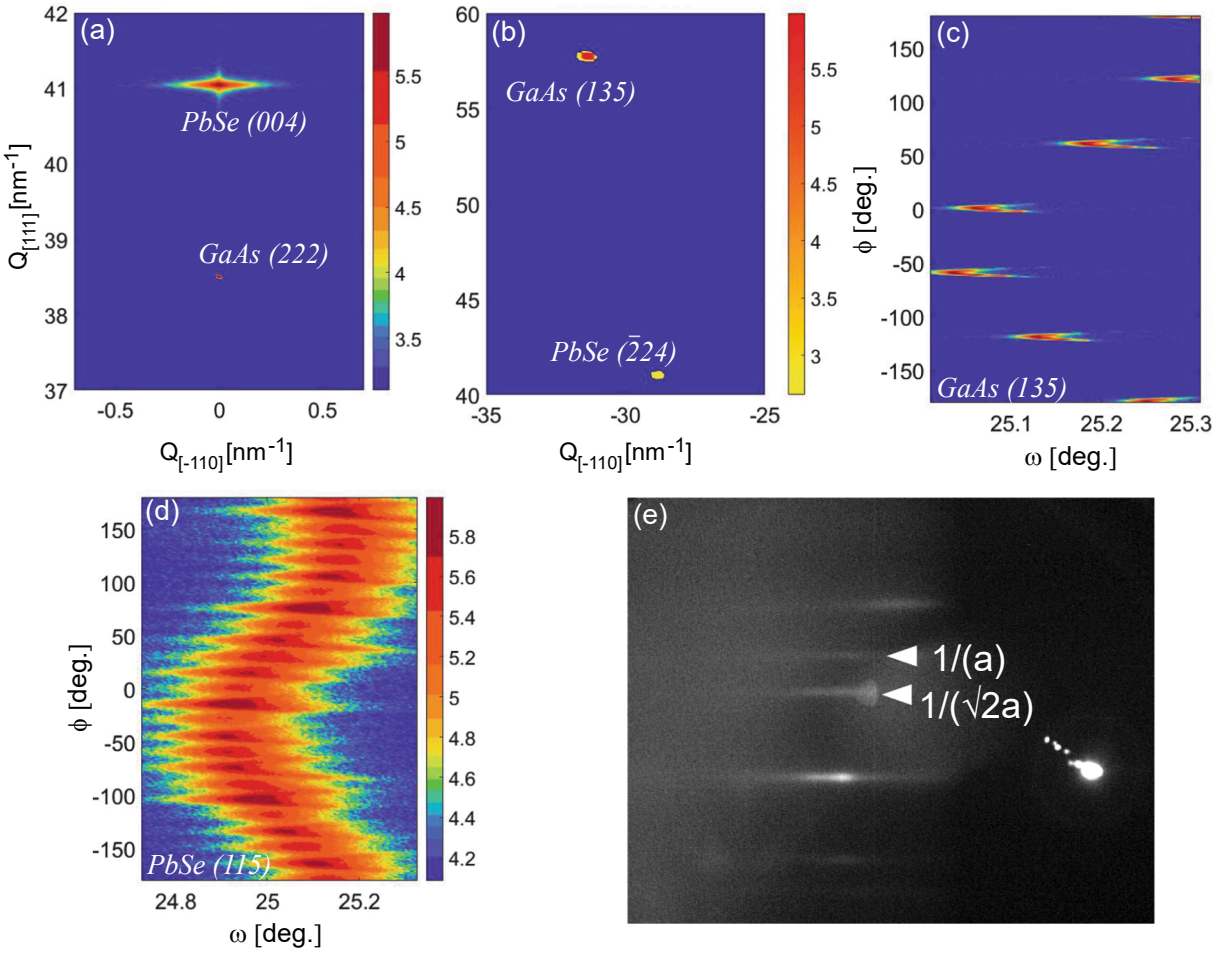

Fig 3. (a) High resolution XRD reciprocal space map of the (2 2 2) Bragg peak of GaAs and the (0 0 4) peak of PbSe. (b) Reciprocal space map showing the (1 3 5) peak of GaAs and ($\bar{2}$24) peak of PbSe. The inset shows a line cut taken at $Q_{[1\,1\,1]} = 41$ nm^{-1} to show the ($\bar{2}$24) peak. ϕ −scan of the (1 3 5) GaAs peak (c) and the (1 1 5) PbSe peak (d). (e) RHEED pattern of PbSe on GaAs(1 1 1) showing streaks corresponding to lattice reciprocal lattice spacings $1/a$ and $1/(\sqrt{2}a)$.

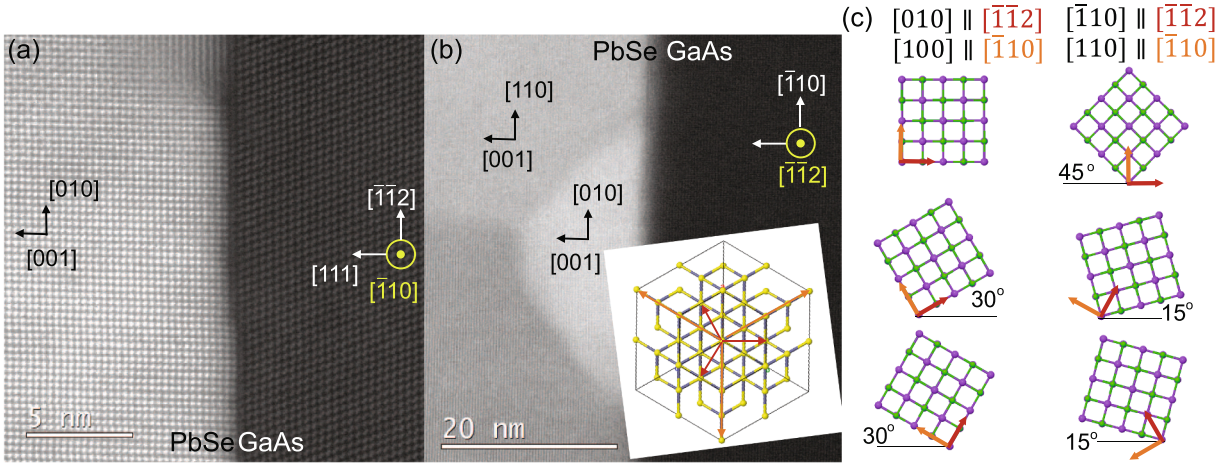

Fig 4. (a) Aberration-corrected annular-dark-field image of PbSe grown on GaAs (1 1 1)B taken along a [$\bar{1}$10] projection. (b) Lower magnification image showing PbSe grains with different in-plane orientation. Inset shows a (1 1 1) plane of GaAs with three possible {1 1 0} directions represented by the orange arrows and three possible {1 1 2} represented by the red arrows. (c)[010]∥[$\bar{1}\bar{1}$2] ([100]∥[$\bar{1}$10]) and $\left[\bar{1}10\right] \| \left[\bar{1}\bar{1}2\right]$ $\left([110] \| [\bar{1}10]\right)$ rocksalt-zincblende in-plane alignment. The first column represents all possible alignments for which the [0 1 0] direction in PbSe is parallel to a [$\bar{1}\bar{1}$2] direction in GaAs. The second column represents all alignments for which the $\left[\bar{1}10\right]$ direction in PbSe is parallel to a $\left[\bar{1}\bar{1}2\right]$ direction in GaAs. (For interpretation of the references to colour in this figure legend, the reader is referred to the web version of this article.)

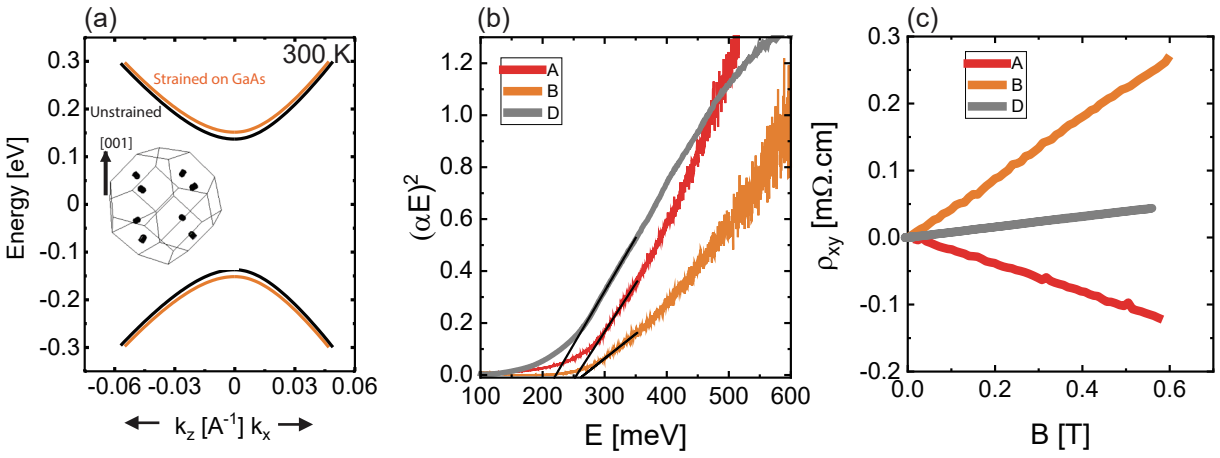

Fig 5. (a) Energy band structure of strained PbSe on GaAs. The inset shows the Brillouin zone of PbSe with 4 ellipsoidal carrier valleys oriented along each ⟨1 1 1⟩ direction. (b) Tauc plot extracted using the absorption coefficient α versus energy obtained from infrared transmission spectroscopy measurements at room temperature. The linear extrapolation used to extract the gap for each sample (solid black lines) is also shown. (c) Hall resistivity versus magnetic field at room temperature.

Fig. 4(b) is a lower magnification image of the same sample but taken along a $[\bar{1}12]$ projection. Two types of grains are visible in PbSe, a region with cubic symmetry corresponding to grains with the [0 1 0]directed parallel to the $[\bar{1}10]$ direction in GaAs (orange in inset Fig. 4(b)) and another that is likely rotated by 45° such that the [1 1 0] direction in PbSe is parallel to $[\bar{1}10]$ of GaAs. Fig. 4(a, b) and the XRD space maps shown in Fig. 3, allow an understanding of the alignment of PbSe on the GaAs(1 1 1) surface as follows: (i) If the [0 1 0] irection of PbSe lines up with the $[\bar{1}12]$ direction of GaAs, then a [1 0 0] direction of PbSe has to necessarily line up with the $[\bar{1}10]$ direction of GaAs. There are, however, three ⟨112⟩ directions yielding 3 possible alignments shown in the first column of Fig. 4(c). For each one of these, there exist 4 possible alignments of the rock-salt unit cell, thus yielding 12 possibilities. (ii) Similarly, the $[\bar{1}10]$ direction of PbSe can lie along the $[\bar{1}12]$ direction of GaAs. In this case, a perpendicular [1 1 0]irection in PbSe will lie along a $[\bar{1}10]$ direction of GaAs. With 3 possible ⟨112⟩ directions shown in the second column of Fig. 4(c) and 4 possible rotations of the rocksalt structure, this alignment will also yield 12 possibilities. Thus, a total of 24 possible alignments are obtained, which explains the ϕ-scan with 24 peaks in Fig. 3(c), as measured by XRD and the mixing observed in the RHEED pattern. No evidence of any misfit dislocations is visible within any single PbSe grain.

3.3. Impact of strain on electronic band properties

The structural analysis performed above indicates that PbSe on GaAs is mainly tensile strained due to the thermal expansion coefficient mismatch but does not exhibit any penetrating bulk defects resulting from lattice mismatch between the two materials.

Thermal strain can alter the band dispersion of PbSe, leading to an increased energy gap. The band structure is computed using the low energy massive Dirac model of IV-VI semiconductors with the parameters measured for PbSe in Ref. [34] and the room temperature energy gap taken from previous literature in the absence of strain ($E_g = 270$ *meV)* [35,36]. It is unclear if this value of E_g includes the Moss-Burstein shift caused by doping. However, this does not impact the interpretation of our results, which focus on the relative change of E_g in the presence of strain. If the conduction and valence band are assumed to be perfectly symmetric, the dispersion is given by [34]:

$$E(k) = \sqrt{\left(\Delta + \frac{\hbar^2 k^2}{2m} + \frac{\hbar k_z^2}{2m_z}\right)^2 + \hbar^2 v^2 k^2 + \hbar^2 v_z^2 k_z^2} \quad (1)$$

Here $\Delta = \frac{E_g}{2} + \delta$, E_g is the energy gap in the absence of strain, δ is a strain induced change in energy gap, $v = 6.45 \times 10^5 m/s$ is the Dirac velocity in the (1 1 1) direction, $v_z^2 = \frac{v^2}{\sqrt{K}}$ is the Dirac velocity perpendicular to the (1 1 1) direction, K = 1.94 for PbSe, $m = 0.23m_0$ and $m_z = 0.32m_0$ [34,37,38]. $\Delta = 135$meV at 293 K. To account for the ellipsoidal Fermi surface (inset in Fig. 5) of PbSe, in this model, the point $k_z = k = 0$ corresponds to an L *−point* in the Brillouin zome, k_z is parallel to a ⟨111⟩ direction and $k = k_x = k_y$ are perpendicular to that direction. PbSe has 4 such valleys: each is ellipsoidal with a great axis oriented along a ⟨111⟩ direction, as illustrated in Fig. 5(a).$\delta$is the strain-induced offset of the energy gap estimated from the elastic constants and deformation potential for PbSe studied in Ref. [33,39]. This model has universally been used to describe IV-VI materials, [37,40,41] at various temperatures. Its representation as a massive Dirac model is a simplification argued for in Ref. [34,42]. Eq. (1) can in fact be directly derived from the matrix Hamiltonian shown in Ref. [37] at zero magnetic field. Moreover,

Table 3
Comparison between the calculated energy gap $E_g + 2\delta$ after the inclusion of strain 2δ (calc.) and the experimental optical gap obtained from the Tauc plot. 2δ(exp.) is found by subtracting the optical gap measured in the control sample D from the gap measured in samples A and B. The measured electrical transport parameters are also shown.

	Sample A	Sample B	Sample D (On BaF_2)
2δ(calc.)	+18 ± 9 meV	+27 ± 13 meV	0
$E_g + 2\delta$	288 meV	297 meV	270 meV (bulk [35,36])
Experimental optical gap	250±10 meV	260±10 meV	220 meV
2δ(exp.)	30 meV	40 meV	–
Carrier density at 300 K	-3×10^{18} cm^{-3}	1.5×10^{18} cm^{-3}	8×10^{18} cm^{-3}
Resistivity at 300 K	0.54 mΩ.m	0.58 mΩ.m	0.037 mΩ.m

according to previous measurements, the parameter that is the most dependent on temperature is Δ. All other parameters vary by negligible amounts [43].

The values of the in-plane and out-of-plane strain extracted from XRD data for samples A and B are shown in Table 1. Using these and the deformation potentials and elastic constant established for PbSe (listed and defined in Table 2), we can compute the change in energy gap δ for biaxial strain in the (1 0 0) plane following [33]:

$$2\delta = 2\varepsilon_{||}\frac{C_{11}-C_{12}}{C_{11}}\left(\frac{D_u^c}{3}-\frac{D_u^v}{3}+D_d^c-D_d^v\right)$$

The resulting band dispersion for sample B is compared to that on unstrained PbSe in Fig. 5(a). The calculated values of the energy gap are shown in Table 3. The strain-induced change of the *gap is found to be between + 20 meV and + 30 meV in PbSe grown on GaAs*.

To confirm this, we carried out FTIR spectroscopy measurements at room temperature in the transmission geometry. The absorption coefficient α is extracted from the transmitted intensity through a given film using the relation:

$$\alpha = -\ln\left(\frac{T_s}{T_b}\right)$$

T_s is the optical transmission intensity as a function of energy E measured through the film and T_b is the transmission measured through the substrate. For semiconductors with a quasi-parabolic dispersion, $\alpha \sim E^{-1/2}$, thus by plotting $(\alpha E)^2$ versus E, we obtain the Tauc plot shown in Fig. 5(b) for sample A and B, and for a control sample D grown on BaF_2. This method has been utilized in the past to extract variations in the energy gap of IV-VI materials, such as PbTe and PbSe, but has been shown to underestimate the gap by more than 50 meV at room temperature [44]. This issue is discussed in a previous work on PbTe and can be due to impurity levels, the Urbach tail visible at low energy and thermal broadening that smear the onset of interband absorption [44,45]. Because of this, we can only make a comparison between the strained samples grown on GaAs and the control sample on BaF_2(1 1 1). The extrapolated optical gaps for the three samples are shown in Table 3. Sample A and B, grown on GaAs yield an energy gap large by 30 to 40 meV compared to sample D grown on BaF_2, in very good agreement with the theoretical calculation.

Lastly, Fig. 5(c) shows the Hall resistivity measured for the three samples A, B and D. The resulting carrier densities are included in Table 3. The carrier density of the sample grown on BaF_2 is slightly larger than that of the two samples on GaAs. The measured change in energy gap between samples A and B, on one hand, and D, on the other, is thus not likely to be due to the Moss-Burstein effect. It is a result of thermal strain from GaAs as theoretically calculated.

4. Conclusions

In summary, we have studied the structural properties of PbSe thin films grown on GaAs (0 0 1) and (1 1 1) substrates. Structurally, GaAs induces a large thermal strain caused by its thermal expansion coefficient being much smaller than that of PbSe. Despite this, the structure of the GaAs-PbSe interface remains nearly pristine, and most dislocations relax within the first few monolayers. For PbSe grown on GaAs(0 0 1), the four-fold cubic symmetry of the rocksalt structure of PbSe is retained. For PbSe grown on GaAs(1 1 1), 6 different alignments of the cubic rocksalt structure on the GaAs (1 1 1) surface are shown to occur. Compared to previous work on the PbSe-III-V [18] interface, our samples retain continuity at room temperature, which results in a finite resistivity (see Table 3) and sustained expansion of the in-plane lattice constant. The resistivity of PbSe grown on GaAs is however lower than that of PbSe grown on the lattice matched BaF_2. The morphology of PbSe on GaAs (0 0 1) seems surprisingly comparable to what was reported for PbSe on InAs(0 0 1) [16]. For the PbSe layer grown on GaAs (1 1 1), the multitude of rotated domains resulting from the symmetry mismatch introduces more morphological disorder. The interface structure remains quite atomically abrupt. Lastly, we have shown that biaxial thermal strain can induce a large change in the energy gap of PbSe, reaching almost 10% of its bulk value, on either GaAs surface. If this strain can be tuned on demand, it can lead to tunable infrared sources and detectors allowing one to vary the characteristic frequency by as much $0.5\mu m$ in the $5\mu m$ mid-infrared range. At a fundamental level, this tuning is important for experiments that aim to control the topological character of $Pb_{1-x}Sn_xSe$ via strain [41,46].

CRediT authorship contribution statement

X. Liu: Conceptualization, Data Curation, Formal analysis, Funding acquisition, Investigation, Methodology, Project administration, Supervision, Visualization, Writing – original draft, Writing – review & editing. **J. Wang:** Formal analysis, Investigation. **L. Riney:** Formal analysis, Investigation. **S.-K. Bac:** Formal analysis, Investigation, Software. **D.J. Smith:** Conceptualization, Data curation, Formal analysis, Funding acquisition, Investigation, Methodology, Project administration, Supervision, Visualization, Writing – original draft, Writing – review & editing. **M.R. McCartney:** Conceptualization, Data curation, Formal analysis, Funding acquisition, Investigation, Methodology, Project administration, Supervision, Visualization, Writing – original draft, Writing – review & editing. **I. Khan:** Formal analysis, Investigation. **A.J. Hoffman:** Formal analysis, Investigation. **M. Dobrowolska:** Project administration, Supervision, Writing – original draft, Writing – review & editing. **J.K. Furdyna:** Project administration, Supervision, Writing – original draft, Writing – review & editing. **B.A. Assaf:** Conceptualization, Data curation, Formal analysis, Funding acquisition, Investigation, Methodology, Project administration, Supervision, Visualization, Writing – original draft, Writing – review & editing.

Declaration of Competing Interest

The authors declare that they have no known competing financial interests or personal relationships that could have appeared to influence the work reported in this paper.

Acknowledgments

This work is supported by NSF-DMR-1905277. JW is partly supported by a seed grant from Notre Dame Nanoscience and Technology (NDnano). DJS and MRM acknowledge use of facilities in the John M. Cowley Center for High Resolution Electron Microscopy at Arizona State University.

The data that support the findings of this study are available from the corresponding author upon reasonable request.

References

[1] P. Dziawa, B.J. Kowalski, K. Dybko, R. Buczko, A. Szczerbakow, M. Szot, E. Łusakowska, T. Balasubramanian, B.M. Wojek, M.H. Berntsen, O. Tjernberg, T. Story, Nat. Mater. 11 (2012) 1023.
[2] S.-Y. Xu, C. Liu, N. Alidoust, M. Neupane, D. Qian, I. Belopolski, J.D.D. Denlinger, Y.J.J. Wang, H. Lin, L.A.A. Wray, G. Landolt, B. Slomski, J.H.H. Dil, A. Marcinkova, E. Morosan, Q. Gibson, R. Sankar, F.C.C. Chou, R.J.J. Cava, A. Bansil, M.Z. Z. Hasan, Nat. Commun. 3 (2012) 1192.
[3] G. Krizman, B.A. Assaf, T. Phuphachong, G. Bauer, G. Springholz, G. Bastard, R. Ferreira, L.A. de Vaulchier, Y. Guldner, Phys. Rev. B 98 (2018), 075303.
[4] B.A. Assaf, T. Phuphachong, V.V. Volobuev, A. Inhofer, G. Bauer, G. Springholz, L. A. De Vaulchier, Y. Guldner, Sci. Rep. 6 (2016) 20323.
[5] S. Chusnutdinow, S. Schreyeck, S. Kret, A. Kazakov, G. Karczewski, Appl. Phys. Lett. 117 (2020), 072102.
[6] M. Khodr, M. Chakraburtty, P.J. McCann, AIP Adv. 9 (2019), 035303.
[7] J.P. Heremans, V. Jovovic, E.S. Toberer, A. Saramat, K. Kurosaki, A. Charoenphakdee, S. Yamanaka, G.J. Snyder, Science 321 (2008) 554.
[8] H. Wang, Y. Pei, A.D. LaLonde, G.J. Snyder, Proc. Natl. Acad. Sci. U. S. A. 109 (2012) 9705.

[9] M.E. Manley, O. Hellman, N. Shulumba, A.F. May, P.J. Stonaha, J.W. Lynn, V. O. Garlea, A. Alatas, R.P. Hermann, J.D. Budai, H. Wang, B.C. Sales, A.J. Minnich, Nat. Commun. 10 (2019) 1928.
[10] H. Zogg, S. Blunier, A. Fach, C. Maissen, P. Müller, S. Teodoropol, V. Meyer, G. Kostorz, A. Dommann, T. Richmond, Phys. Rev. B 50 (1994) 10801.
[11] G. Springholz, in Mol. Beam Ep., edited by M. Henini (Elsevier, 2013), pp. 263–310.
[12] H. Clemens, H. Krenn, B. Tranta, P. Ofner, G. Bauer, Superlattices Microstruct. 4 (1988) 591.
[13] J. Sadowski, M.A. Herman, J. Cryst. Growth 146 (1995) 449.
[14] M. Shandalov, Y. Golan, Eur. Phys. J. Appl. Phys. 28 (2004) 51.
[15] M. Shandalov, Y. Golan, Eur. Phys. J. Appl. Phys. 24 (2003) 13.
[16] B.B. Haidet, E.T. Hughes, K. Mukherjee, Phys. Rev. Mater. 4 (2020), 033402.
[17] X.J. Wang, Y.B. Hou, Y. Chang, C.R. Becker, R.F. Klie, T.W. Kang, R. Sporken, S. Sivananthan, J. Cryst. Growth 311 (2009) 2359.
[18] H. Clemens, P. Ofner, G. Bauer, J.M. Hong, L.L. Chang, Mater. Lett. 7 (1988) 127.
[19] R.A. Snyder, C.J. Trimble, C.C. Rong, P.A. Folkes, P.J. Taylor, J.R. Williams, Phys. Rev. Lett. 121 (2018), 097701.
[20] M. Cubukcu, H.J. von Bardeleben, K. Khazen, J.L. Cantin, O. Mauguin, L. Largeau, A. Lemaître, Phys. Rev. B 81 (2010), 041202.
[21] X. Li, S.K. Bac, S.N. Dong, X.Y. Liu, S. Lee, S. Rouvimov, M. Dobrowolska, J. K. Furdyna, Aip Adv. 8 (2018) 56401.
[22] C. Brüne, C.X. Liu, E.G. Novik, E.M. Hankiewicz, H. Buhmann, Y.L. Chen, X.L. Qi, Z.X. Shen, S.C. Zhang, L.W. Molenkamp, Phys. Rev. Lett. 106 (2011), 126803.
[23] M. Goyal, H. Kim, T. Schumann, L. Galletti, A.A. Burkov, S. Stemmer, Phys. Rev. Mater. 3 (2019), 064204.
[24] V.V. Volobuev, P.S. Mandal, M. Galicka, O. Caha, J. Sánchez-Barriga, D. Di Sante, A. Varykhalov, A. Khiar, S. Picozzi, G. Bauer, P. Kacman, R. Buczko, O. Rader, G. Springholz, Adv. Mater. 29 (2017) 1604185.
[25] E. Plekhanov, P. Barone, D. Di Sante, S. Picozzi, Phys. Rev. B 90 (2014), 161108.
[26] S. Jin, H. Wu, T. Xu, Appl. Phys. Lett. 95 (2009), 132105.
[27] P.J. McCann, J. Fuchs, Z. Feit, C.G. Fonstad, J. Appl. Phys. 62 (1987) 2994.
[28] H. Gobrecht, A. Richter, J. Phys. Chem. Solids 26 (1965) 1889.
[29] D.R. Lide, CRC Handbook of Chemistry and Physics, 79th Editi, CRC Press, Boca Raton, FL, 1998.
[30] H. Preier, Appl. Phys. 20 (1979) 189.
[31] S. Vishwanath, X.Y. Liu, S. Rouvimov, L. Basile, N. Lu, A. Azcatl, K. Magno, R. M. Wallace, M. Kim, J.C. Idrobo, J.K. Furdyna, D. Jena, H.G. Xing, J. Mater. Res. 31 (2016) 900.
[32] G. Springholz and D. R. Khokhlov, in Optoelectron. Prop. Semicond. Superlattices (Taylor and Francis Books, Inc., New York, NY, 2002), pp. 123–207.
[33] I. I. Zasavitskii, E. A. de Andrada e Silva, E. Abramof, and P. J. McCann, Phys. Rev. B 70, 115302 (2004).
[34] G. Krizman, B.A. Assaf, T. Phuphachong, G. Bauer, G. Springholz, L.A. de Vaulchier, Y. Guldner, Phys. Rev. B 98 (2018), 245202.
[35] M. Baleva, T. Georgiev, G. Lashkarev, J. Phys. Condens. Matter 2 (1990) 2935.
[36] A.J. Strauss, Phys. Rev. 157 (1967) 608.
[37] G. Bauer, in Narrow Gap Semicond. Phys. Appl. Proceeding Int. Summer Sch., edited by W. Zawadzki (Springer Berlin Heidelberg, Berlin, Heidelberg, 1980), pp. 427–446.
[38] J. Melngailis, T.C. Harman, W.C. Kernan, Phys. Rev. B 5 (1972) 2250.
[39] M. Simma, G. Bauer, G. Springholz, Phys. Rev. B 90 (2014), 195310.
[40] J.O. Dimmock, k.p theory for the conduction and valence bands of Pb1-xSnxTe and Pb1-xSnxSe alloys, in: D.L. Carter, R.T. Bates (Eds.), Proceedings of the International Conference on the Physics of Semimetals and Narrow Gap Semiconductors, 1971, p. 319.
[41] T.H. Hsieh, H. Lin, J. Liu, W. Duan, A. Bansil, L. Fu, Nat. Commun. 3 (2012) 982.
[42] T. Liang, Q. Gibson, J. Xiong, M. Hirschberger, S.P. Koduvayur, R.J. Cava, N. P. Ong, Nat. Commun. 4 (2013) 3696.
[43] B.M. Wojek, P. Dziawa, B.J. Kowalski, A. Szczerbakow, A.M. Black-Schaffer, M. H. Berntsen, T. Balasubramanian, T. Story, O. Tjernberg, Phys. Rev. B 90 (2014).
[44] Z.M. Gibbs, A. LaLonde, G.J. Snyder, New J. Phys. 15 (2013), 075020.
[45] F. Stern, J. Appl. Phys. 32 (1961) 2166.
[46] G. Krizman, B. A. Assaf, G. Bauer, G. Springholz, R. Ferreira, G. Bastard, L.-A. de Vaulchier, and Y. Guldner, in Terahertz Emit. Receiv. Appl. X, edited by M. Razeghi, A. N. Baranov, and M. S. Vitiello (SPIE, 2019), p. 26.